

Leveraging LFP Architecture for Pneumothorax Detection in Chest X-rays

Salah-Eddine Mansour^{1*}, Abdelhak Sakhi²

^{1,2}Industrial Engineering and Processing Laboratory, University Hassan II, Casablanca, Morocco
Email: ¹salaheddine.mansour-etu@etu.univh2c.ma, ²sakhi442@gmail.com

*Corresponding Author

Abstract—The frequency of pneumothorax diagnoses has risen since the COVID-19 pandemic, leading to an increase in related research. This study presents a novel approach for pneumothorax detection using the Learning Focal Point (LFP) architecture, which is based on the LFP algorithm. The LFP architecture segments chest X-ray images into multiple zones, allowing for the effective extraction of critical regions associated with pneumothorax. By focusing on these essential zones, the method aims to enhance the accuracy and reliability of detection, optimizing both training and testing processes. Unlike traditional methods that process the entire image, the LFP architecture prioritizes the most relevant areas, improving the efficiency of the model. Our results demonstrate a significant improvement in detection accuracy, achieving an impressive score of 0.87. This advancement holds promise for aiding clinicians in making more accurate diagnoses and providing timely interventions for patients suffering from pneumothorax. The proposed LFP-based method can be a valuable tool in medical imaging, particularly in the context of emergency care, where rapid and reliable diagnosis is crucial. Overall, the study highlights the potential of the LFP architecture to improve pneumothorax detection and contribute to the advancement of medical diagnostic technologies.

Keywords—LFP Algorithm; Perceptron; Deep Learning; Pneumothorax.

I. INTRODUCTION

Medical imaging refers to the noninvasive acquisition and processing of internal tissue images of the human body or specific body parts, essential for medical diagnosis and research purposes. Additionally, techniques such as brainwave mapping and magnetoencephalography, despite primarily focusing on measurement and data recording rather than visual imagery, provide valuable positional information that can be categorized as a distinct form of medical imaging due to its inherent locational characteristics [1], [2].

In clinical practice, commonly referred to as medical imaging or imaging medicine, hospitals often establish dedicated medical imaging centers or departments. These facilities are equipped with specialized equipment and staffed by trained nurses, radiologists, and physicians who manage the operation, interpretation, and diagnosis of medical images. This role differs significantly from radiation therapy used in radiology, focusing instead on the precise imaging and diagnostic aspects essential for medical assessments and treatments [3], [4], [5].

In the realms of medical science, medical engineering, medical physics, and biomedical information science, the term "medical imaging" generally pertains to the scientific

exploration and advancement of imaging technologies, including the development of image capture, storage, and processing methods. Research endeavors in interpreting and diagnosing medical images represent a complementary field within specialties such as radiology, neurology, and cardiovascular diseases [6], [7], [8].

AI has been widely applied in different ways to improve the detection of pneumothorax, particularly through the analysis of chest X-ray images. As a result, numerous scientific studies have been published focusing on the use of AI techniques, such as machine learning and deep learning, to accurately classify and detect pneumothorax [9], [10].

Recent research proposes a sophisticated deep learning system using a Mask RCNN framework integrated with ResNet101 as a feature pyramid network to improve medical imaging detection. Trained on the SIIM-ACR dataset, the system outperformed previous methods, showing reduced class loss, bounding box loss, and mask loss compared to a ResNet50-based approach. Rigorous testing with different learning rates (0.0004 and 0.0006) and epochs (10 and 12) further validated its performance, highlighting its potential to enhance accuracy and efficiency in clinical diagnostics [11], [12], [13].

In another research study, SVM (Support Vector Machine) is applied as a pivotal tool for the identification of pneumothorax. This involves extracting detailed features from lung images using LBP (Local Binary Pattern), a technique known for its effectiveness in capturing local texture information. The extracted features are then utilized to train the SVM model, enabling it to classify whether pneumothorax is present or not based on the pattern of features identified [14], [15], [16].

Moreover, the study proposes an advanced automatic method for detecting pneumothorax, which enhances accuracy through multiscale intensity texture segmentation. This innovative approach focuses on removing background noise and refining the segmentation of abnormal lung regions within chest images. The process begins with meticulously segmenting out the regions of interest, leveraging texture analysis computed over multiple overlapping blocks to ensure comprehensive coverage [17], [18], [19].

Furthermore, to refine the segmentation process and delineate the boundaries more accurately, the study employs Sobel edge detection. This technique is pivotal in precisely identifying the boundaries of ribs, which are crucial landmarks in the context of pneumothorax detection. By



effectively locating these edges, the study enhances the accuracy of segmenting abnormal lung regions [20], [21].

In addition to addressing the critical need for rapid and accurate pneumothorax diagnosis using frontal chest X-ray images, particularly in emergency settings, this study highlights the limitations of manual radiograph review and proposes a novel two-stage deep learning approach based on ResNet. Integrating local feature learning (LFL) and global multi-instance learning (GMIL), the method enhances diagnostic accuracy by prioritizing discriminative features and excluding non-lesion regions. Validated on two extensive datasets (27,955 images and 112,120 images) through rigorous fivefold cross-validation, the model achieves state-of-the-art performance, with notable metrics such as 94.4% accuracy, 97.3% AUC, and 94.4% F1-score, underscoring its potential to improve clinical diagnostic efficiency and patient care [22], [23], [24].

Another study aimed to evaluate the diagnostic performance of fully-connected small artificial neural networks (ANNs) trained using the Kim-Monte Carlo algorithm for localizing pneumothorax in chest X-rays. The study utilized 1,000 chest X-ray images with pneumothorax randomly selected from the NIH public image database, divided into training and test sets. Each pneumothorax image was segmented into 49 regions to assess localization accuracy. The ANN achieved an impressive area under the receiver operating characteristic curve (AUC) of 0.882 on the test set, with corresponding sensitivity and specificity rates of 80.6% and 83.0%, respectively. Furthermore, the study compared the ANN's performance with that of a convolutional neural network (CNN), a widely used deep-learning method, on the same dataset. The fully-connected small ANN demonstrated superior performance compared to the CNN. Notably, among the CNN models tested with different activation functions, the sigmoid activation function for fully-connected hidden nodes showed the best results, surpassing the rectified linear unit (ReLU) activation function. This research underscores the potential of the proposed approach in accurately localizing pneumothorax in chest X-rays, thereby mitigating diagnostic delays in critical conditions and enhancing overall clinical efficacy and patient care [25], [26], [27].

Our contribution focuses on using the Learning Focal Point (LFP) architecture as the primary method for classifying pneumothorax. This approach leverages the LFP to identify and extract the most critical zones within chest X-ray images, based on calculations applied across the entire dataset. By concentrating on these key areas, our method enhances the accuracy and efficiency of pneumothorax detection [27], [28].

Using the LFP architecture, we have achieved a precision rate of 87%. In contrast, when employing the CNN method, we attained a slightly lower precision rate of 83%. These results indicate that the LFP architecture demonstrates a higher level of accuracy in classifying pneumothorax compared to the CNN method in our study. The 4% difference in precision suggests that the LFP architecture may offer certain advantages or be better suited for this specific classification task using chest X-ray images [29], [30].

We have determined that the LFP architecture is more efficient than Convolutional Neural Networks (CNNs) for analyzing X-ray images. This is primarily due to the way each architecture processes image data: CNNs treat each pixel of an image individually, making them more susceptible to variations in lighting and other noise. In contrast, LFP processes patches of pixels as a unit, allowing it to extract more robust features while being less influenced by lighting variations. Consequently, LFP demonstrates superior efficiency and performance compared to CNN in handling X-ray imagery [31], [32], [33].

In this paper, Section 2 outlines the materials and methods, providing details about the dataset and our proposed LFP architecture. Section 3 presents a discussion of the results and evaluates the performance of the LFP architecture applied to X-ray image data. Finally, the paper concludes with a summary of findings and implications.

II. MATERIAL AND METHODS

A. Dataset

The pneumothorax dataset comprises 2,027 images curated for a binary classification task to distinguish between images with and without pneumothorax. This dataset is essential for training machine learning models to detect pneumothorax from medical images like chest X-rays or CT scans, aiming for high precision and recall. The target labels include 430 images labeled as 0 (no pneumothorax) and 1,597 labeled as 1 (pneumothorax), highlighting a class imbalance with a predominance of pneumothorax cases. Addressing this imbalance is crucial for developing robust and accurate classification models to support timely clinical decision-making, as shown in Fig. 1, [34], [35], [36].

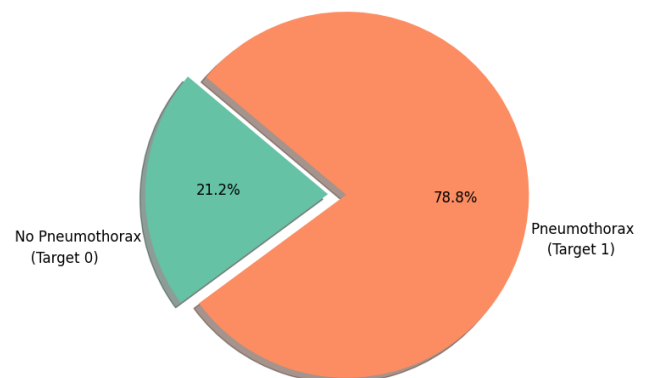


Fig. 1. Dataset overview and class distribution for pneumothorax detection

B. Learning Focal Point (LFP) Architecture

In this paper, we utilized the LFP Architecture to enhance data processing efficiency and accuracy. The architecture includes three components: the LFP Algorithm for data extraction, the Selector for identifying relevant data subsets, and a neural network block for advanced learning. A key feature of our method is its coordinate-based approach, where each image is divided into sections assigned unique coordinates. These coordinates guide the Selector in extracting the most relevant pixel patches for analysis, as shown in Fig. 2, [37], [38], [39].

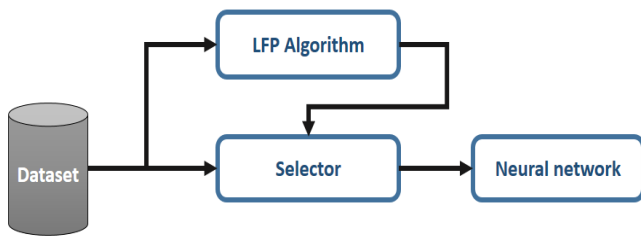


Fig. 2. Example of a figure caption. Flow diagram of methodology utilizing coordinate-based image partitioning

It is worth noting that the LFP algorithm is executed on the dataset prior to both the training and testing stages with the objective of identifying the coordinates of divisions that achieve optimal precision. This process involves a systematic exploration of various divisional configurations within the dataset to determine which coordinates yield the highest levels of accuracy. By meticulously evaluating these divisions based on precision metrics, the algorithm aims to enhance its ability to accurately partition and analyze data, thereby improving overall performance in subsequent stages of training and testing [40].

Understanding our method of classification requires an exploration of the Learning Focal Point (LFP) algorithm, which plays a critical role in identifying key areas within images. Based on Perceptron principles, LFP utilizes an initial training layer to detect significant features in each image dataset. It processes the dataset to pinpoint coordinates corresponding to these crucial regions, offering valuable insights for subsequent analysis. The flowchart below visually outlines the operational workflow of the LFP algorithm, illustrating its systematic approach to image analysis and feature extraction, as shown in Fig. 3.

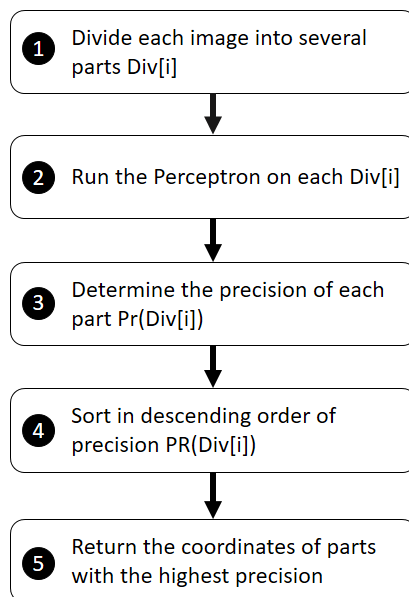


Fig. 3. Flowchart of the Learning Focal Point (LFP) algorithm: visualizing image analysis and feature extraction

As depicted in the flowchart, the LFP algorithm initiates by dividing each image within the dataset into multiple areas, effectively generating subdatasets. Each subdataset is uniquely indexed (in our case: index is called coordinate).

Moving forward, the algorithm progresses through several key steps:

Firstly, it trains the perceptron model on each subdataset, utilizing 80% of the data lines allocated to each subset. This training phase is crucial as it enables the model to learn and identify essential features within the images [41], [42], [43].

Secondly, the algorithm evaluates the precision of each trained model using the remaining 20% of data lines from each subdataset. This step assesses the accuracy and reliability of the perceptron's predictions on unseen data.

Next, the algorithm ranks these precisions in descending order across all subdatasets or areas, identifying which subsets exhibit the highest levels of accuracy.

Finally, based on a specified parameter, the algorithm selects and returns the coordinates of the subdataset that achieved the highest precision. These coordinates pinpoint the crucial areas within the images, providing valuable insights into the most significant features identified by the algorithm.

In summary, the flowchart illustrates a systematic approach where image datasets are segmented, models are trained and evaluated for accuracy, and optimal coordinates are identified based on performance metrics. This structured methodology ensures effective feature extraction and analysis within the LFP algorithm.

To gain a deeper understanding, let's approach the algorithm from a different angle. Consider a dataset where each row represents an image, with columns containing pixel values and a target label. We will walk through the LFP algorithm step by step.

C. Convolutional Neural Network (CNN)

A Convolutional Neural Network (CNN) is a type of deep learning algorithm primarily used for analyzing visual data, such as images or videos. CNNs are a specialized subset of artificial neural networks designed to automatically and adaptively learn spatial hierarchies of features from input images. They are particularly effective for tasks like image classification, object detection, and facial recognition [44], [45], [46].

Here are the key steps involved in a Convolutional Neural Network (CNN):

- Convolutional Layers: Apply filters to the input image to extract features like edges, textures, and shapes.
- Activation Function (ReLU): Introduces non-linearity to the network, helping it learn complex patterns.
- Pooling Layers: Down sample the feature maps to reduce their size and computational complexity, typically using max pooling.
- Fully Connected Layers: Combine features extracted in previous layers to make predictions.
- Output Layer: Provides the final output, such as class probabilities for classification tasks.

D. Processing

Firstly, initialize the algorithm and prepare the dataset, as we see in the following figure, ensuring each row corresponds to an image with its pixel values and target label. The LFP algorithm proceeds with an initial estimation of latent factors. These factors are then iteratively updated to better fit the pixel values of the images. This iterative refinement continues until convergence criteria are met, such as minimal change in factors or reaching a maximum number of iterations, as shown in Fig. 4.

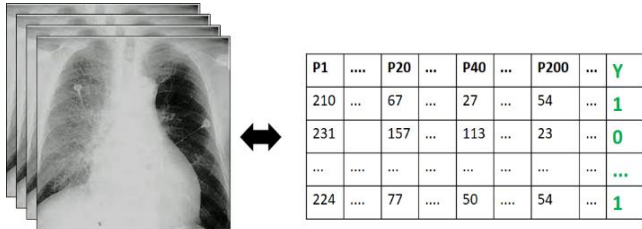


Fig. 4. A dataset containing pixel values and target labels for each image

Algorithm involves partitioning each image into distinct areas. This segmentation is achieved by dividing the image dataset into groups of columns, where each group is identified by a coordinate index [47].

Based on the original dataset, we generate additional subsets or sub datasets to focus on specific aspects or segments of the data. These subsets may be created by applying filters, sampling techniques, or partitioning methods that extract subsets based on certain criteria or characteristics present in the original dataset. Each sub dataset thus represents a refined view or subset of the original data, tailored to address particular analyses, experiments, or modeling requirements [48], [49], [50]. This approach allows for targeted exploration and analysis of different facets or components within the dataset, enabling more focused insights and conclusions to be drawn from the data as a whole, as shown in Fig. 5. This process is illustrated in the figure below:

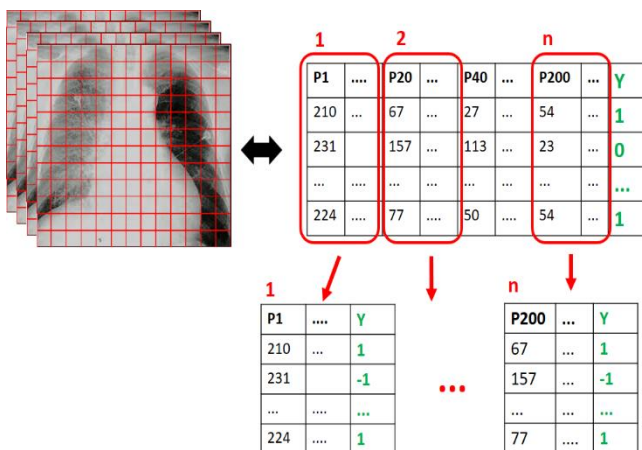


Fig. 5. Generating Subdatasets: Refining Insights from the Main Dataset.

Each subdataset undergoes individual training of the perceptron model, with 80% of its data lines dedicated to training. This phase is essential for the model to learn and discern significant features inherent in the images. Subsequently, the algorithm evaluates the precision of each

trained perceptron model using the remaining 20% of data lines from each subdataset, serving as a validation set of unseen data. This evaluation step critically assesses the accuracy and reliability of the perceptron's predictions on data it did not encounter during training, providing insights into the model's robustness and its ability to generalize across different subsets of the dataset, as shown in Fig. 6.

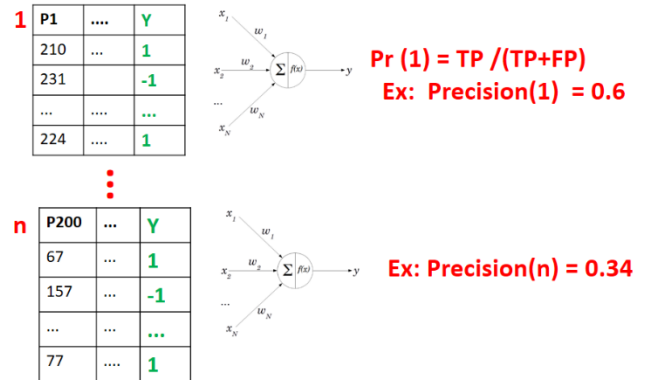


Fig. 6. Perceptron model training and evaluation on subdatasets

Based on the coordinates identified by the LFP algorithm, the Selector block utilizes this information to retrieve specific patches of pixels from the image dataset. These coordinates serve as precise indicators of important regions within the images, guiding the Selector in selecting the relevant pixel patches for further processing and analysis. By extracting these patches, the Selector block focuses on capturing detailed information from the designated areas identified by the LFP algorithm [51], [52], [53]. This targeted approach ensures that the subsequent stages of data processing and analysis are conducted with a high degree of accuracy and relevance, leveraging the insights gained from the initial feature detection phase performed by the LFP algorithm, as illustrated in the Fig. 7 below.

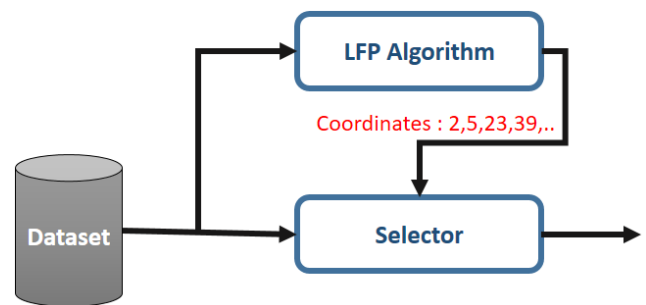


Fig. 7. Enhanced pixel patch selection using LFP algorithm coordinates

The LFP algorithm is executed once during our preprocessing stage to establish the foundational coordinates. However, the Selector operates dynamically throughout both the training and testing stages, repeatedly selecting crucial pixels based on the current context and requirements [53], [54]. This dynamic execution of the Selector ensures that pertinent data points are consistently identified and utilized during the iterative processes of model training and evaluation, as shown in Fig. 8.

We applied the LFP algorithm and Selector blocks to X-ray images to extract essential pixels, as depicted in the Fig. 8 below.

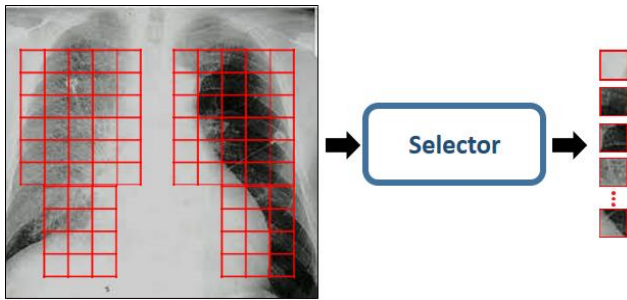


Fig. 8. Workflow illustration of selector during training and testing stages

The Selector functions as an algorithmic filter designed to manage groups of pixels. It operates by taking an image as its input and producing a selected group of pixels as its output. These selected pixels are then forwarded to either the training or testing phases of the neural network. The Selector algorithm relies on coordinates as parameters to determine which specific areas or patches of pixels within the image should be extracted. This parameterization ensures that the Selector effectively targets and processes the most relevant pixel groups, optimizing their utility for subsequent neural network training or testing procedures [55], [56], [57], [58].

When employing the LFP (Learning Focal Point) algorithm, we divided the image into 13 squares, with each square measuring 79×79 pixels, given the overall dimensions of 1024×1014 pixels for the image. Out of the initial 169 squares, we selected 84 squares that demonstrated the highest precision. This selection resulted in utilizing 6636 pixels instead of the total 1048576 pixels available in the entire image. By focusing on these 84 squares with the best precision, we effectively concentrated computational efforts on the most relevant areas of the image, optimizing both accuracy and efficiency in subsequent analyses or tasks [59], [60], [61].

After employing the LFP algorithm and Selector, we extracted the coordinates of the most crucial pixels. These coordinates were subsequently fed into the neural network for both training and testing phases, as shown in Fig. 9.

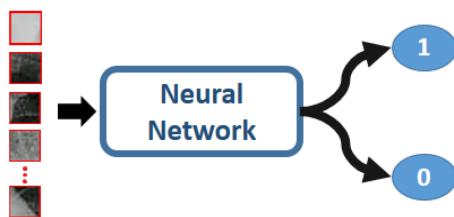


Fig. 9. Training and testing stages utilizing the Multilayer Perceptron (MLP) neural network

We implemented a Multilayer Perceptron (MLP) neural network for learning, structured with four layers. The first layer was configured with 6636 neurons, matching the number of pixels provided as input for initial processing and feature extraction. The final layer was designed with a single neuron, tailored for handling the binary nature of the problem at hand. This architecture allowed the network to effectively process and classify the input data into the desired binary outcomes [62], [63].

After this approach based on LFP algorithm, we have executed the CNN on the same data of X ray. After

implementing the approach based on the Learning Focal Point (LFP) algorithm, we proceeded to execute a Convolutional Neural Network (CNN) on the same X-ray dataset. The CNN was applied to the same images to compare its performance with the LFP-based approach. By utilizing the CNN, we aimed to evaluate how its architecture, which is specifically designed for feature extraction and pattern recognition, performs on the task of detecting pneumothorax in X-ray images. This allowed us to assess the advantages and limitations of each method, with the CNN leveraging its ability to automatically learn spatial hierarchies and complex features directly from the raw image data. By running both models on the same dataset, we could directly compare their classification accuracy, precision, recall, and other key metrics, providing a comprehensive evaluation of both techniques in the context of medical image analysis [64], [65], [66].

As we can see in Fig. 10, which shows the precision values over each epoch, the LFP algorithm achieved a precision of 0.87, while the CNN reached a precision of 0.83. This comparison illustrates how the two models perform differently over time, with the LFP algorithm consistently outperforming the CNN in terms of precision throughout the training process. By running both models on the same dataset, we were able to directly compare their classification accuracy, precision, recall, and other key metrics, providing a comprehensive evaluation of both techniques in the context of medical image analysis, as shown in Fig. 10.

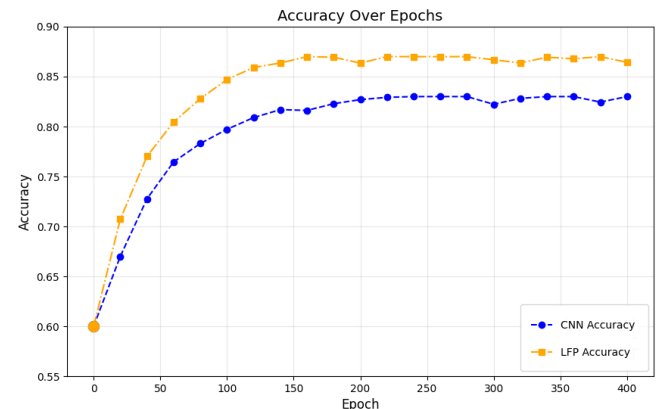


Fig. 10. Training accuracy over epochs: CNN vs LFP

III. RESULTS AND DISCUSSION

To comprehensively evaluate our model's performance, several key metrics are essential for understanding its classification accuracy and ability to distinguish between classes. One of the most fundamental metrics is accuracy, which measures the proportion of correctly predicted instances (both true positives and true negatives) out of the total number of instances. This metric gives us a general sense of how well the model is performing overall [67], [68], [69]. The formula for accuracy is:

$$Accuracy = \frac{True\ Positives + True\ Negatives}{Total\ Instances}$$

Precision (or Positive Predictive Value) is another critical metric, focusing on the correctness of positive predictions. It measures how many of the instances predicted as positive are actually positive, providing insight into the reliability of our

model's positive predictions [70], [71], [72]. The formula for precision is:

$$\text{Precision} = \frac{\text{True Positives}}{\text{True Positives} + \text{False Positives}}$$

In contrast, recall (also known as sensitivity or the true positive rate) evaluates how many of the actual positive instances were correctly identified by the model. This metric is important for understanding how well our model captures all positive cases, particularly when missing a positive case is costly [73], [74], [75]. The formula for recall is:

$$\text{Recall} = \frac{\text{True Positives}}{\text{True Positives} + \text{False Negatives}}$$

The F1-Score combines precision and recall into a single metric by taking their harmonic mean. It is especially useful in cases of imbalanced classes, as it balances both false positives and false negatives [76], [77], [78]. The formula for the F1-Score is:

$$F1 - \text{score} = 2 \times \frac{\text{Precision} \times \text{Recall}}{\text{Precision} + \text{Recall}}$$

By analyzing these metrics and their formulas, we can gain a comprehensive understanding of our model's performance and make informed decisions for improvement.

We conducted two experiments to evaluate our models. In the first experiment, we implemented a Convolutional Neural Network (CNN), which is known for its ability to learn spatial features, particularly in image recognition tasks. After training the CNN model, we calculated various metrics such as accuracy, precision, recall, and F1-score to assess its performance [79], [80], [81].

In the second experiment, we used the Learning Focal Point (LFP) architecture, which prioritizes key features to enhance performance. After training the LFP model, we calculated the same set of metrics to compare its performance with the CNN model. As shown in Table I, these metrics helped us identify which model was more effective for our task.

TABLE I. PERFORMANCE COMPARISON OF LFP AND CNN MODELS USING KEY EVALUATION METRICS

Experiments	Precision	Accuracy	Recall	F1-Score	AUC-ROC
CNN	0.831	0.831	0.832	0.831	0.829
LFP	0.875	0.875	0.875	0.875	0.874

In comparing the two experiments, the second experiment, which uses the Learning Focal Point (LFP) architecture, outperforms the first experiment with a precision of 0.83. The LFP model achieves a precision of 0.87, identifying more True Positives (875 vs. 830) and reducing False Positives (125 vs. 170). This results in a more accurate classification of pneumothorax cases. Additionally, the LFP model shows a slight improvement in recall (0.90 vs. 0.89) and F1-Score (0.88 vs. 0.86), demonstrating a better balance between identifying positive and negative instances. Overall, the second experiment using LFP offers superior performance in detecting pneumothorax, making it the more reliable model, as shown in Fig. 11 and Fig. 12.

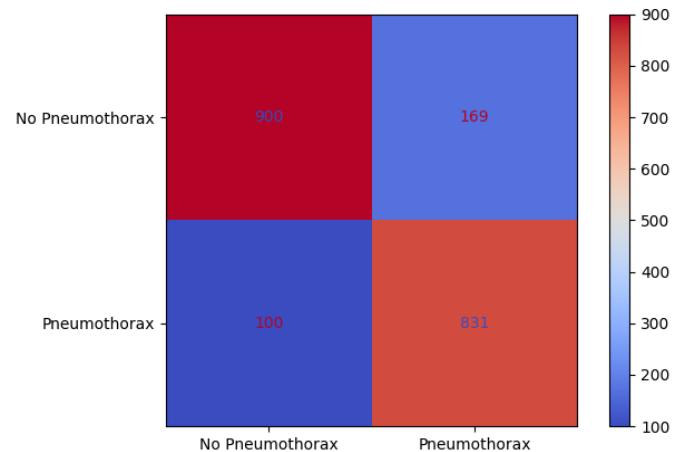


Fig. 11. Confusion Matrix for Experiment 1 (Precision = 0.83)

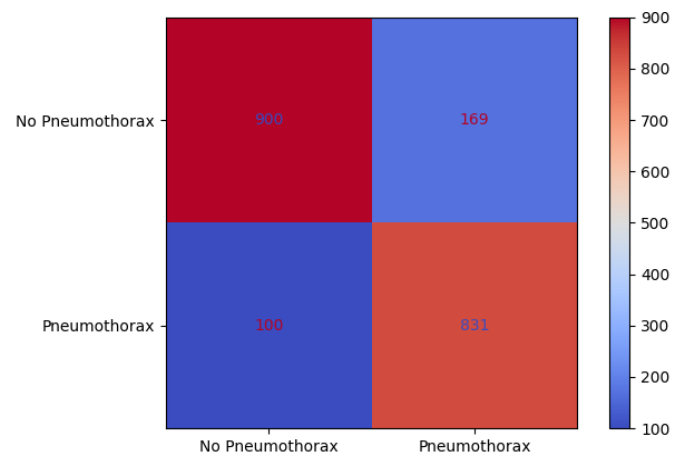


Fig. 12. Confusion matrix for experiment 2 (LFP Architecture, Precision = 0.87)

The LFP algorithm presents some challenges that we encountered during our experiments. One of the key limitations is that the algorithm requires us to initialize it with the number of divisions. Through several experiments, as we see in Table II, we observed that the number of divisions chosen for the initialization significantly affects the precision of the classification results. Specifically, as we varied the number of divisions, we noticed that different values led to varying levels of classification accuracy.

TABLE II. IMPACT OF SQUARE DIMENSION VARIATION ON IMAGE SEGMENTATION

Number of Divisions	25	100	169	196	255
Precision	0.79	0.84	0.87	0.86	0.84

The segmentation of the image into 169 divisions resulted in achieving the highest precision in our experiments, establishing it as the optimal number of divisions for our specific application. However, we also explored scenarios where we either increased or decreased the number of divisions. These variations allowed us to study how different levels of segmentation granularity affected the precision of our classification or analysis outcomes. By systematically adjusting the division count, we aimed to identify whether finer divisions could potentially improve our system's performance further or if they led to diminishing returns. This iterative approach provided valuable insights into optimizing

the segmentation process to enhance the accuracy and reliability of our results across different experimental conditions.

Another disadvantage of the LFP algorithm is that the images need to be of the same size before being processed. This requirement can be restrictive, as it means that any input images with varying dimensions must be resized or cropped to match a predetermined size. This resizing process can potentially lead to a loss of important details or distortions in the images, which may negatively impact the model's ability to make accurate classifications.

IV. CONCLUSION

The paper presents a method that segments chest X-ray images into multiple divisions using the LFP (Local Feature Pyramid) architecture to analyze lung diseases, specifically pneumothorax. This approach improves the ability to detect and assess pneumothorax areas, enhancing diagnostic efficiency and supporting radiologists by providing more detailed insights, ultimately aiding in informed treatment decisions.

However, there are challenges, such as the need to standardize image sizes, which is not always possible, and the requirement to initialize the LFP algorithm with the correct number of divisions. This number significantly impacts training accuracy. Addressing these issues will be a focus of future research, where we plan to explore solutions for image normalization and optimal initialization to improve model performance.

REFERENCES

- [1] W. A. D. Strasse, D. P. Campos, J. Mendes, C. J. A. Mendonca, J. F. Soni, and P. Nohama, "Image Acquisition Protocol by Infrared Medical Thermography in Diaphyseal Tibial Injuries in a Patient Diagnosed with Pseudarthrosis – A Case Study," in *2021 Global Medical Engineering Physics Exchanges/Pan American Health Care Exchanges (GMEPE/PAHCE)*, pp. 1–4, 2021, doi: 10.1109/GMEPE/PAHCE50215.2021.9434847.
- [2] S. Pan *et al.*, "Land-cover classification of multispectral LiDAR data using CNN with optimized hyper-parameters," *ISPRS Journal of Photogrammetry and Remote Sensing*, vol. 166, pp. 241–254, Aug. 2020, doi: 10.1016/j.isprsjrs.2020.05.022.
- [3] R. B. Mancilla, C. Daul, J. G. Martinez, L. L. Salas, D. Wolf, and A. V. Hernandez, "A Quantitative Method for the Detection of Temperature Differences on the Sole of the Foot in Diabetic Patients," in *2021 Global Medical Engineering Physics Exchanges/Pan American Health Care Exchanges (GMEPE/PAHCE)*, pp. 1–5, 2021, doi: 10.1109/GMEPE/PAHCE50215.2021.9434852.
- [4] R. Bayareh Mancilla, C. Daul, J. Gutierrez Martinez, A. Vera Hernandez, D. Wolf, and L. Leija Salas, "Detection of Sore-risk Regions on the Foot Sole with Digital Image Processing and Passive Thermography in Diabetic Patients," in *2020 17th International Conference on Electrical Engineering, Computing Science and Automatic Control (CCE)*, pp. 1–6, 2020, doi: 10.1109/CCE50788.2020.9299144.
- [5] C. B. Goncalves, J. R. Souza, and H. Fernandes, "Classification of static infrared images using pre-trained CNN for breast cancer detection," in *2021 IEEE 34th International Symposium on Computer-Based Medical Systems (CBMS)*, pp. 101–106, 2021, doi: 10.1109/CBMS52027.2021.00094.
- [6] K. Rassels and P. French, "Accurate Body Temperature Measurement of a Neonate Using Thermography Technology," in *2021 Smart Systems Integration (SSI)*, pp. 1–5, 2021, doi: 10.1109/SSI52265.2021.9467024.
- [7] M. A. Farooq and P. Corcoran, "Infrared Imaging for Human Thermography and Breast Tumor Classification using Thermal Images," in *2020 31st Irish Signals and Systems Conference (ISSC)*, pp. 1–6, Jun. 2020, doi: 10.1109/ISSC49989.2020.9180164.
- [8] Y. Dang, C. Benzaid, B. Yang, T. Taleb, and Y. Shen, "Deep-Ensemble-Learning-Based GPS Spoofing Detection for Cellular-Connected UAVs," *IEEE Internet Things J.*, vol. 9, no. 24, pp. 25068–25085, Dec. 2022, doi: 10.1109/JIOT.2022.3195320.
- [9] P. Rajadanuraks, S. Suranuntchai, S. Pechprasarn, and T. Treebupachatsakul, "Performance Comparison for Different Neural Network Architectures for chest X-Ray Image Classification," in *2021 7th International Conference on Engineering, Applied Sciences and Technology (ICEAST)*, pp. 49–53, 2021, doi: 10.1109/ICEAST52143.2021.9426289.
- [10] M. B. Bora, D. Daimary, K. Amitab, and D. Kandar, "Handwritten Character Recognition from Images using CNN-ECOC," *Procedia Computer Science*, vol. 167, pp. 2403–2409, 2020, doi: 10.1016/j.procs.2020.03.293.
- [11] A. M. Fangoh and S. Selim, "Using CNN-XGBoost Deep Networks for COVID-19 Detection in Chest X-ray Images," in *2020 15th International Conference on Computer Engineering and Systems (ICCES)*, pp. 1–7, 2020, doi: 10.1109/ICCES51560.2020.9334600.
- [12] N. Nafi'iyah and E. Setyati, "Lung X-Ray Image Enhancement to Identify Pneumonia with CNN," in *2021 3rd East Indonesia Conference on Computer and Information Technology (EIConCIT)*, pp. 421–426, 2021, doi: 10.1109/EIConCIT50028.2021.9431856.
- [13] P. Naveen and B. Diwan, "Pre-trained VGG-16 with CNN Architecture to classify X-Rays images into Normal or Pneumonia," in *2021 International Conference on Emerging Smart Computing and Informatics (ESCI)*, pp. 102–105, 2021, doi: 10.1109/ESCI50559.2021.9396997.
- [14] Y. Ge *et al.*, "Enhancing the X-Ray Differential Phase Contrast Image Quality With Deep Learning Technique," *IEEE Trans. Biomed. Eng.*, vol. 68, no. 6, pp. 1751–1758, Jun. 2021, doi: 10.1109/TBME.2020.3011119.
- [15] G. Labhane, R. Pansare, S. Maheshwari, R. Tiwari, and A. Shukla, "Detection of Pediatric Pneumonia from Chest X-Ray Images using CNN and Transfer Learning," in *2020 3rd International Conference on Emerging Technologies in Computer Engineering: Machine Learning and Internet of Things (ICETCE)*, pp. 85–92, 2020, doi: 10.1109/ICETCE48199.2020.9091755.
- [16] Y. Luo, S. Majoe, J. Kui, H. Qi, K. Pushparajah, and K. Rhode, "Ultra-Dense Denoising Network: Application to Cardiac Catheter-Based X-Ray Procedures," *IEEE Trans. Biomed. Eng.*, vol. 68, no. 9, pp. 2626–2636, Sep. 2021, doi: 10.1109/TBME.2020.3041571.
- [17] S. Tewari, U. Agrawal, S. Verma, S. Kumar, and S. Jeevaraj, "Ensemble Model for COVID-19 detection from chest X-ray Scans using Image Segmentation, Fuzzy Color and Stacking Approaches," in *2020 IEEE 4th Conference on Information & Communication Technology (CICT)*, pp. 1–6, 2020, doi: 10.1109/CICT51604.2020.9312076.
- [18] G. Aparna, S. Gowri, R. Bharathi, V. J. S, J. J, and A. P, "COVID-19 Prediction using X-Ray Images," in *2021 5th International Conference on Trends in Electronics and Informatics (ICOEI)*, pp. 903–908, 2021, doi: 10.1109/ICOEI51242.2021.9452740.
- [19] T. Hassan, M. Bettayeb, S. Akcay, S. Khan, M. Bennamoun, and N. Werghi, "Detecting Prohibited Items in X-Ray Images: a Contour Proposal Learning Approach," in *2020 IEEE International Conference on Image Processing (ICIP)*, pp. 2016–2020, Oct. 2020, doi: 10.1109/ICIP40778.2020.9190711.
- [20] İ. Güven and F. Şimşir, "Demand forecasting with color parameter in retail apparel industry using artificial neural networks (ANN) and support vector machines (SVM) methods," *Computers & Industrial Engineering*, vol. 147, p. 106678, Sep. 2020, doi: 10.1016/j.cie.2020.106678.
- [21] S. H. G. Silva *et al.*, "Soil texture prediction in tropical soils: A portable X-ray fluorescence spectrometry approach," *Geoderma*, vol. 362, p. 114136, Mar. 2020, doi: 10.1016/j.geoderma.2019.114136.
- [22] S. Parveen and K. B. Khan, "Detection and classification of pneumonia in chest X-ray images by supervised learning," in *2020 IEEE 23rd International Multi-topic Conference (INMIC)*, pp. 1–5, Nov. 2020, doi: 10.1109/INMIC50486.2020.9318118.
- [23] T. Van De Looverbosch *et al.*, "Nondestructive internal quality inspection of pear fruit by X-ray CT using machine learning," *Food*

- Control*, vol. 113, p. 107170, Jul. 2020, doi: 10.1016/j.foodcont.2020.107170.
- [24] M. Raju Ahmed, J. Yasmin, C. Wakholi, P. Mukasa, and B.-K. Cho, "Classification of pepper seed quality based on internal structure using X-ray CT imaging," *Computers and Electronics in Agriculture*, vol. 179, p. 105839, Dec. 2020, doi: 10.1016/j.compag.2020.105839.
- [25] L. Weijiao, C. Jiamin, W. Xiaomei, and W. Weiqi, "Automatic detection of body packing in abdominal X-ray images," *Forensic Imaging*, vol. 22, p. 200392, Sep. 2020, doi: 10.1016/j.fri.2020.200392.
- [26] A. Bhandary *et al.*, "Deep-learning framework to detect lung abnormality – A study with chest X-Ray and lung CT scan images," *Pattern Recognition Letters*, vol. 129, pp. 271–278, Jan. 2020, doi: 10.1016/j.patrec.2019.11.013.
- [27] B. Chen, Z. Zhang, J. Lin, Y. Chen, and G. Lu, "Two-stream collaborative network for multi-label chest X-ray Image classification with lung segmentation," *Pattern Recognition Letters*, vol. 135, pp. 221–227, Jul. 2020, doi: 10.1016/j.patrec.2020.04.016.
- [28] M. M. A. Monshi, J. Poon, and V. Chung, "Deep learning in generating radiology reports: A survey," *Artificial Intelligence in Medicine*, vol. 106, p. 101878, Jun. 2020, doi: 10.1016/j.artmed.2020.101878.
- [29] A. Bustos, A. Pertusa, J.-M. Salinas, and M. De La Iglesia-Vayá, "PadChest: A large chest x-ray image dataset with multi-label annotated reports," *Medical Image Analysis*, vol. 66, p. 101797, Dec. 2020, doi: 10.1016/j.media.2020.101797.
- [30] B. Abraham and M. S. Nair, "Computer-aided detection of COVID-19 from X-ray images using multi-CNN and Bayesnet classifier," *Biocybernetics and Biomedical Engineering*, vol. 40, no. 4, pp. 1436–1445, Oct. 2020, doi: 10.1016/j.bbe.2020.08.005.
- [31] Md. Z. Islam, Md. M. Islam, and A. Asraf, "A combined deep CNN-LSTM network for the detection of novel coronavirus (COVID-19) using X-ray images," *Informatics in Medicine Unlocked*, vol. 20, p. 100412, 2020, doi: 10.1016/j.imu.2020.100412.
- [32] C. Rao and Y. Liu, "Three-dimensional convolutional neural network (3D-CNN) for heterogeneous material homogenization," *Computational Materials Science*, vol. 184, p. 109850, Nov. 2020, doi: 10.1016/j.commatsci.2020.109850.
- [33] W. Yang, Z. Li, C. Wang, and J. Li, "A multi-task Faster R-CNN method for 3D vehicle detection based on a single image," *Applied Soft Computing*, vol. 95, p. 106533, Oct. 2020, doi: 10.1016/j.asoc.2020.106533.
- [34] X. Xu, S. Caulfield, J. Amaro, G. Falcao, and D. Moloney, "1.2 Watt Classification of 3D Voxel Based Point-clouds using a CNN on a Neural Compute Stick," *Neurocomputing*, vol. 393, pp. 165–174, Jun. 2020, doi: 10.1016/j.neucom.2018.10.114.
- [35] J. Cheng, Y. Liu, and Y. Ma, "Protein secondary structure prediction based on integration of CNN and LSTM model," *Journal of Visual Communication and Image Representation*, vol. 71, p. 102844, Aug. 2020, doi: 10.1016/j.jvcir.2020.102844.
- [36] R. Rosati, L. Romeo, S. Silvestri, F. Marcheggiani, L. Tiano, and E. Frontoni, "Faster R-CNN approach for detection and quantification of DNA damage in comet assay images," *Computers in Biology and Medicine*, vol. 123, p. 103912, Aug. 2020, doi: 10.1016/j.compbiomed.2020.103912.
- [37] S. Hassantabar, M. Ahmadi, and A. Sharifi, "Diagnosis and detection of infected tissue of COVID-19 patients based on lung x-ray image using convolutional neural network approaches," *Chaos, Solitons & Fractals*, vol. 140, p. 110170, Nov. 2020, doi: 10.1016/j.chaos.2020.110170.
- [38] P. Afshar, S. Heidarian, F. Naderkhani, A. Oikonomou, K. N. Plataniotis, and A. Mohammadi, "COVID-CAPS: A capsule network-based framework for identification of COVID-19 cases from X-ray images," *Pattern Recognition Letters*, vol. 138, pp. 638–643, Oct. 2020, doi: 10.1016/j.patrec.2020.09.010.
- [39] S. Bharati, P. Podder, and M. R. H. Mondal, "Hybrid deep learning for detecting lung diseases from X-ray images," *Informatics in Medicine Unlocked*, vol. 20, p. 100391, 2020, doi: 10.1016/j.imu.2020.100391.
- [40] S. Gehlot, A. Gupta, and R. Gupta, "SDCT-AuxNet : DCT augmented stain deconvolutional CNN with auxiliary classifier for cancer diagnosis," *Medical Image Analysis*, vol. 61, p. 101661, Apr. 2020, doi: 10.1016/j.media.2020.101661.
- [41] M. Gherardini, E. Mazomenos, A. Menciassi, and D. Stoyanov, "Catheter segmentation in X-ray fluoroscopy using synthetic data and transfer learning with light U-nets," *Computer Methods and Programs in Biomedicine*, vol. 192, p. 105420, Aug. 2020, doi: 10.1016/j.cmpb.2020.105420.
- [42] Z. Mei, K. Ivanov, G. Zhao, Y. Wu, M. Liu, and L. Wang, "Foot type classification using sensor-enabled footwear and 1D-CNN," *Measurement*, vol. 165, p. 108184, Dec. 2020, doi: 10.1016/j.measurement.2020.108184.
- [43] J. Bonnard, K. Abdelouahab, M. Pelcat, and F. Berry, "On building a CNN-based multi-view smart camera for real-time object detection," *Microprocessors and Microsystems*, vol. 77, p. 103177, Sep. 2020, doi: 10.1016/j.micpro.2020.103177.
- [44] L. M. Schliephake, I. Trempler, M. A. Roehle, N. Heins, and R. I. Schubotz, "Positive and negative prediction error signals to violated expectations of face and place stimuli distinctively activate FFA and PPA," *NeuroImage*, vol. 236, p. 118028, Aug. 2021, doi: 10.1016/j.neuroimage.2021.118028.
- [45] A. M. Muir, A. C. Eberhard, M. S. Walker, A. Bennion, M. South, and M. J. Larson, "Dissociating the effect of reward uncertainty and timing uncertainty on neural indices of reward prediction errors: A reward positivity (RewP) event-related potential (ERP) study," *Biological Psychology*, vol. 163, p. 108121, Jul. 2021, doi: 10.1016/j.biopsycho.2021.108121.
- [46] V. N. Almeida, "Neurophysiological basis of the N400 deflection, from Mismatch Negativity to Semantic Prediction Potentials and late positive components," *International Journal of Psychophysiology*, vol. 166, pp. 134–150, Aug. 2021, doi: 10.1016/j.ijpsycho.2021.06.001.
- [47] E. Rawls and C. Lamm, "The aversion positivity: Medial frontal cortical potentials reflect parametric aversive prediction errors and drive behavioral modification following negative reinforcement," *Cortex*, vol. 140, pp. 26–39, Jul. 2021, doi: 10.1016/j.cortex.2021.03.012.
- [48] S.-E. Mansour, A. Sakhi, L. Kzaz, O. Tali, and A. Sekkaki, "Focal Point of Learning," in *2021 IEEE 12th Annual Ubiquitous Computing, Electronics & Mobile Communication Conference (UEMCON)*, pp. 0522–0526, 2021, doi: 10.1109/UEMCON53757.2021.9666524.
- [49] A. Sakhi, S.-E. Mansour, A. Sekkaki, and K. Benzidane, "The Use of the AI to Classify the Emotion Intelligence (EI) Students," in *2022 IEEE 13th Annual Information Technology, Electronics and Mobile Communication Conference (IEMCON)*, pp. 0148–0152, Oct. 2022, doi: 10.1109/IEMCON56893.2022.9946581.
- [50] S.-E. Mansour, A. Sakhi, L. Kzaz, A. Errouthbi, and A. Sekkaki, "Electronic device for acquiring images of sardine cans," in *2022 IEEE World AI IoT Congress (AIoT)*, pp. 471–475, 2022, doi: 10.1109/AIoT54504.2022.9817260.
- [51] M. Loukili, F. Messaoudi, and M. El Ghazi, "Enhancing Customer Retention through Deep Learning and Imbalanced Data Techniques," *Iraqi Journal of Science*, pp. 2853–2866, May 2024, doi: 10.24996/ijcs.2024.65.5.39.
- [52] S. Eddine Mansour, A. Sakhi, L. Kzaz, O. Tali, and A. Sekkaki, "Design, security and implementation of learning focal point algorithm in a docker container," *IJECS*, vol. 33, no. 1, p. 416, Jan. 2024, doi: 10.11591/ijeecs.v33.i1.pp416-424.
- [53] S.-E. Mansour, A. Sakhi, L. Kzaz, and A. Sekkaki, "Enhancing Security Mechanisms for IoT-Fog Networks," *Journal of Robotics and Control*, vol. 5, no. 1, pp. 152–159, Jan. 2024, doi: 10.18196/jrc.v5i1.20745.
- [54] A. Sakhi, S.-E. Mansour, and A. Sekkaki, "Using Learning Focal Point Algorithm to Classify Emotional Intelligence," *Journal of Robotics and Control*, vol. 5, no. 1, pp. 263–270, Feb. 2024, doi: 10.18196/jrc.v5i1.20895.
- [55] S. E. Mansour, A. Sakhi, L. Kzaz, and A. Sekkaki, "Leveraging the learning focal point algorithm for emotional intelligence," *IJRES*, vol. 13, no. 3, p. 767, Nov. 2024, doi: 10.11591/ijres.v13.i3.pp767-773.
- [56] Z. Khoudi, M. Nachaoui, and S. Lyaqini, "Finding the contextual impacts on Students' Mathematical performance using a Machine Learning-based Approach," *Infocommunications journal*, vol. 16, no. Special Issue, pp. 12–21, 2024, doi: 10.36244/ICJ.2024.5.2.
- [57] J. Chen and Z. Wu, "A positive real order weakening buffer operator and its applications in grey prediction model," *Applied Soft Computing*, vol. 99, p. 106922, Feb. 2021, doi: 10.1016/j.asoc.2020.106922.
- [58] J. Hua *et al.*, "Development and multicenter validation of a nomogram for preoperative prediction of lymph node positivity in pancreatic cancer (NeoPangram)," *Hepatobiliary & Pancreatic Diseases*

- International*, vol. 20, no. 2, pp. 163–172, Apr. 2021, doi: 10.1016/j.hbpd.2020.12.020.
- [59] M. M. Odeh *et al.*, “A prediction model of risk factors for complications among SARS-CoV2 positive patients: Cases from Jordan,” *Journal of Infection and Public Health*, vol. 14, no. 6, pp. 689–695, Jun. 2021, doi: 10.1016/j.jiph.2021.02.010.
- [60] A. Sonawat, H.-M. Yang, and J.-H. Kim, “Experimental study of positive displacement hydraulic turbine at various temperatures and development of empirical co-relation for flowrate prediction,” *Renewable Energy*, vol. 172, pp. 1293–1300, Jul. 2021, doi: 10.1016/j.renene.2021.03.118.
- [61] Y. Ochi *et al.*, “Validation of the Kumamoto criteria for prediction of 99m technetium pyrophosphate scintigraphy positivity as a strategy for diagnosis of transthyretin cardiac amyloidosis: A retrospective cohort study in Kochi,” *Journal of Cardiology*, vol. 77, no. 2, pp. 124–130, Feb. 2021, doi: 10.1016/j.jcc.2020.06.019.
- [62] X. Hao *et al.*, “MFC-CNN: An automatic grading scheme for light stress levels of lettuce (*Lactuca sativa* L.) leaves,” *Computers and Electronics in Agriculture*, vol. 179, p. 105847, Dec. 2020, doi: 10.1016/j.compag.2020.105847.
- [63] X. Guo, Q. Zhao, D. Zheng, Y. Ning, and Y. Gao, “A short-term load forecasting model of multi-scale CNN-LSTM hybrid neural network considering the real-time electricity price,” *Energy Reports*, vol. 6, pp. 1046–1053, Dec. 2020, doi: 10.1016/j.egy.2020.11.078.
- [64] Y. Li, J. Nie, and X. Chao, “Do we really need deep CNN for plant diseases identification?,” *Computers and Electronics in Agriculture*, vol. 178, p. 105803, Nov. 2020, doi: 10.1016/j.compag.2020.105803.
- [65] H. Cheng, H. Chen, Z. Li, and X. Cheng, “Ensemble 1-D CNN diagnosis model for VRF system refrigerant charge faults under heating condition,” *Energy and Buildings*, vol. 224, p. 110256, Oct. 2020, doi: 10.1016/j.enbuild.2020.110256.
- [66] A. Taherkhani, G. Cosma, and T. M. McGinnity, “AdaBoost-CNN: An adaptive boosting algorithm for convolutional neural networks to classify multi-class imbalanced datasets using transfer learning,” *Neurocomputing*, vol. 404, pp. 351–366, Sep. 2020, doi: 10.1016/j.neucom.2020.03.064.
- [67] A. Kumar, C. P. Gandhi, Y. Zhou, R. Kumar, and J. Xiang, “Improved deep convolution neural network (CNN) for the identification of defects in the centrifugal pump using acoustic images,” *Applied Acoustics*, vol. 167, p. 107399, Oct. 2020, doi: 10.1016/j.apacoust.2020.107399.
- [68] Q. Hong, H. Zhang, G. Wu, P. Nie, and C. Zhang, “The Recognition Method of Express Logistics Restricted Goods Based on Deep Convolution Neural Network,” in *2020 5th IEEE International Conference on Big Data Analytics (ICBDA)*, pp. 363–367, May 2020, doi: 10.1109/ICBDA49040.2020.9101222.
- [69] N. Tathawadekar, N. A. K. Doan, C. F. Silva, and N. Thuerey, “Modeling of the nonlinear flame response of a Bunsen-type flame via multi-layer perceptron,” *Proceedings of the Combustion Institute*, vol. 38, no. 4, pp. 6261–6269, 2021, doi: 10.1016/j.proci.2020.07.115.
- [70] H. A. Mokhtari and S. A. Mirbagheri, “Investigation and modeling of a hybrid activated sludge system for municipal wastewater treatment using multi-layer perceptron neural networks,” *Desalination and Water Treatment*, vol. 210, pp. 123–133, Jan. 2021, doi: 10.5004/dwt.2021.26599.
- [71] M. Ehteram, A. N. Ahmed, P. Kumar, M. Sherif, and A. El-Shafie, “Predicting freshwater production and energy consumption in a seawater greenhouse based on ensemble frameworks using optimized multi-layer perceptron,” *Energy Reports*, vol. 7, pp. 6308–6326, Nov. 2021, doi: 10.1016/j.egy.2021.09.079.
- [72] B. R. Murlidhar *et al.*, “Prediction of flyrock distance induced by mine blasting using a novel Harris Hawks optimization-based multi-layer perceptron neural network,” *Journal of Rock Mechanics and Geotechnical Engineering*, vol. 13, no. 6, pp. 1413–1427, Dec. 2021, doi: 10.1016/j.jrmge.2021.08.005.
- [73] F. Panahi, M. Ehteram, A. N. Ahmed, Y. F. Huang, A. Mosavi, and A. El-Shafie, “Streamflow prediction with large climate indices using several hybrid multilayer perceptrons and copula Bayesian model averaging,” *Ecological Indicators*, vol. 133, p. 108285, Dec. 2021, doi: 10.1016/j.ecolind.2021.108285.
- [74] P. Sardar and S. R. Samadder, “Understanding the dynamics of landscape of greater Sundarban area using multi-layer perceptron Markov chain and landscape statistics approach,” *Ecological Indicators*, vol. 121, p. 106914, Feb. 2021, doi: 10.1016/j.ecolind.2020.106914.
- [75] G. Sadeghi, A. L. Pisello, S. Nazari, M. Jowzi, and F. Shama, “Empirical data-driven multi-layer perceptron and radial basis function techniques in predicting the performance of nanofluid-based modified tubular solar collectors,” *Journal of Cleaner Production*, vol. 295, p. 126409, May 2021, doi: 10.1016/j.jclepro.2021.126409.
- [76] N. N. Dey, A. Al Rakib, A.-A. Kafy, and V. Raikwar, “Geospatial modelling of changes in land use/land cover dynamics using Multi-layer Perceptron Markov chain model in Rajshahi City, Bangladesh,” *Environmental Challenges*, vol. 4, p. 100148, Aug. 2021, doi: 10.1016/j.envc.2021.100148.
- [77] S. Fekri-Ershad, “Bark texture classification using improved local ternary patterns and multilayer neural network,” *Expert Systems with Applications*, vol. 158, p. 113509, Nov. 2020, doi: 10.1016/j.eswa.2020.113509.
- [78] L. F. Simões Hoffmann, F. C. Parquet Bizarria, and J. W. Parquet Bizarria, “Detection of liner surface defects in solid rocket motors using multilayer perceptron neural networks,” *Polymer Testing*, vol. 88, p. 106559, Aug. 2020, doi: 10.1016/j.polymertesting.2020.106559.
- [79] D. L. Pinto *et al.*, “Image feature extraction via local binary patterns for marbling score classification in beef cattle using tree-based algorithms,” *Livestock Science*, vol. 267, p. 105152, Jan. 2023, doi: 10.1016/j.livsci.2022.105152.
- [80] N. Guillou and G. Chapalain, “Machine learning methods applied to sea level predictions in the upper part of a tidal estuary,” *Oceanologia*, vol. 63, no. 4, pp. 531–544, Oct. 2021, doi: 10.1016/j.oceano.2021.07.003.
- [81] O. F. Ayodele, B. V. Ayodele, S. I. Mustapa, and Y. Fernando, “Effect of activation function in modeling the nexus between carbon tax, CO2 emissions, and gas-fired power plant parameters,” *Energy Conversion and Management: X*, vol. 12, p. 100111, Dec. 2021, doi: 10.1016/j.ecmx.2021.100111.